# Unlocking the Potential of Antisolvent-Free Perovskite Solar Cells: Modulating Crystallization and Intermediates through a Binary Volatile Additive Strategy

Bo Zhou[a], Pei Zhao[b], Junxue Guo[a,c], Yu Qiao[a], Shuaifeng Hu[d], Xin Guo[a], Jiewei Liu[a,*], Can Li[a,c,*]

---

[a] *State Key Laboratory of Catalysis, Dalian National Laboratory for Clean Energy, Dalian Institute of Chemical Physics, Chinese Academy of Sciences, Dalian 116023, China*

[b] *Research Center for Computational Science, Institute for Molecular Science, Okazaki 444-8585, Japan*

[c] *School of Chemistry and Materials Science, University of Science and Technology of China, Hefei 230026, China*

[d] *Clarendon Laboratory, Department of Physics, University of Oxford, Parks Road, Oxford OX1 3PU, U.K.*

* Corresponding author.

*E-mail addresses:* jwliu@dicp.ac.cn (J. Liu), canli@dicp.ac.cn (C. Li)

## Abstract:

High-quality perovskite polycrystalline thin films are generally achieved through antisolvent-assisted crystallization, a crucial process that facilitates desolvation. However, antisolvent method is limited by issues of toxicity and fabrication complexity. Here, we introduce a “binary volatile additive” strategy using methylammonium chloride (MACl) and trifluoroacetamide (TFAA) in dimethylformamide/N-methyl-2-pyrrolidone co-solvent system, enabling end-to-end management of antisolvent-free crystallization process. Combining in-situ characterizations and DFT calculations, we prove that TFAA adjusts coordination with perovskite intermediates, facilitating solvent removal and promoting the formation of nuclei, while MACl reduces the formation energy of α-phase formamidinium-based perovskite. Moreover, TFAA not only releases the residual strain caused by MACl, but also in combination with MACl, synergistically widens crystallization window and regulates ripening process, allowing for precise fabrication of homogeneous perovskite films with suppressed defects. By employing the “binary volatile additive” approach, we achieve perovskite solar cells with a power conversion efficiency up to 22.4% and elongated storage life (93% PCE retention over 1000 hours). Our study offers a simple and sustainable approach to produce high-quality perovskite films without the acquisition of antisolvent, streamlining the fabrication process.

## Keywords:

Binary volatile additives; Crystallization window; Intermediates; Perovskite solar cells; Antisolvent-free

## 1. Introduction

Over the past decade, organic-inorganic metal halide perovskite solar cells (PSCs) have garnered immense interest, achieving certified highest power conversion efficiencies (PCE) of 26.1% [1]. For formamidinium (FA)-based perovskites such as $FAPbI_3$ or $(FACs)PbI_3$, which are more favorable concerning stability, one-step method with an antisolvent quenching process is commonly used for fabricating efficient and stable PSCs [2]. However, this method presents challenges for industrial-scale production due to compatibility issues with large-area coating techniques, narrow processing windows, and concerns regarding device reproducibility [3,4]. Furthermore, commonly used antisolvents like chlorobenzene and toluene raise toxicity concerns [5,6]. Hence, developing an antisolvent-free approach is urgently needed to produce high-quality perovskite films.

To this end, several antisolvent-free methods have been explored, such as the introduction of volatile solvents like acetonitrile (ACN) [7] and 2-methoxyethanol (2-ME) [8], which can naturally evaporate during the thin film deposition process. However, the potential of solvent engineering is limited by restricted applicability due to the disadvantages associated with volatile, non-coordinating solvents, such as their rapid nucleation rates, low polarity and limited solvent capacity [9]. Unlike common highly polar solvents, e.g., dimethylformamide (DMF) and dimethylsulfoxide (DMSO), the low solvating power of the volatile solvents not only prevents complete dissolution of perovskites but also makes the intermediate phase less stable at room temperature [10]. As a result, the key to achieve an antisolvent-free method lies in balancing solvation and desolvation processes. Alternatively, N-methyl-2-pyrrolidone (NMP), a non-volatile coordinating solvent, can effectively modulate the intermediate phases due to strong polarity and is also widely utilized in the fabrication of antisolvent-free perovskite solar cells (PSCs) [11-13]. Gao et al. demonstrated the weak intermolecular interactions between NMP and DMF, along with strong coordination with $PbI_2$ and FAI precursors [14]. This facilitated the formation of the intermediate phase and induced rapid DMF evaporation during spin-coating in NMP/DMF co-solvent systems. Similarly, Huang et al. reported the formation of a $PbI_2$•NMP complex that underwent in-situ reaction with embedded FAI species during mixed-solvent evaporation, effectively lowering the formation energy of $\alpha$-$FAPbI_3$ perovskite [15]. Thus, employing DMF/NMP as the basic co-solvent system enables the one-step deposition of perovskite films without the need for antisolvent.

Besides processing solvent, crystallization window is another significant parameter for obtaining high-quality perovskite films. In the high-speed coating process, rapid solvent removal offers fabrication simplicity and preparation efficiency, but often leads to short crystallization window and thus non-dense perovskite films with defects, low reproducibility, and inferior device performance. To tackle this issue, additives have been employed to slow down the crystallization process. The addition of methylammonium chloride (MACl) has been widely utilized to enhance the crystallization of the intermediate phase and stabilize the desired $\alpha$-phase in perovskite materials [16]. MACl facilitates the $\alpha$-phase transition at lower temperatures [17], but the lattice shrinkage caused by its strong dipole effect introduces additional compressive strain [18]. Additionally, binary microcrystalline additives have been proposed, where pre-synthesized microcrystals serve as nucleation seeds for $FAPbI_3$-based perovskite growth [19]. Therefore, additive engineering is considered as an effective approach for achieving a thorough management of crystallization process and passivating defects. However, there is still lack of the introduction of multifunctional molecules [20] into antisolvent-free fabrication methods, and the comprehensive interaction mechanism between additives and solvents requires further exploration.

In this study, we incorporate binary volatile additives, MACl and trifluoroacetamide (TFAA) [21,22], into a self-volatilization perovskite precursor mixed with DMF/NMP to fabricate $FA_{0.9}Cs_{0.1}Pb(I_xCl_{1-x})_3$ perovskite films, and elucidate the crystallization mechanism in this antisolvent-free system. TFAA, with three functional groups ($–CF_3$, $–NH_3$, and –C=O), can potentially bind with $Pb^{2+}$, making it a versatile additive that passivates grain boundaries and surface defects [23]. Experimental and theoretical evidences demonstrate that TFAA can regulate the intermediate phase transition and promote NMP detachment through covalent and hydrogen bonding, thereby increasing nucleation density and slowing down the subsequent growth. Its underlying mechanism involves interactions between the $PbI_2$•NMP adducts, facilitating partial NMP solvent exchange. Our research reveals that, the inclusion of ionic additive MACl lowers the formation energy of $\alpha$-phases, while the multifunctional additive TFAA interact with FAI•$PbI_2$•NMP intermediate, both leading to the formation of more nuclei and the extension of the ripening process [24,25]. The volatility plays a crucial role in promoting the ripening process and grain boundary passivation. During the process, TFAA also releases the compressive strain caused by MACl. Together, the binary additives broaden the crystallization window, which allows us to fabricate the perovskite films with increased grain size and supressed deffect states via this antisolvent-free sustaninable fabraication route. The resulting PSCs achieved a power conversion efficiency (PCE) up to 22.4%, highlighting the effectiveness of the binary additive approach in an antisolvent-free technique. Additionally, the optimized devices exhibited substantially improved storage stability, with approximately 93% of the initial efficiency maintained over 1000 hours of storage in ambient air (25 ºC, 35±5% relative humidity).

## 2. Results and Discussion

### *2.1. Crystallization Kinetics of Perovskite Film with Additives*

The quality of perovskite layers is largely determined by nucleation process, driven by supersaturation and growth controlled by diffusion, including the transformation of intermediate phases during solution drying. To better understand the effects of mixed solvents and additives on perovskite film formation during solution processing, we studied the perovskite films fabricated with (target) or without (control) binary additives in precursor solution.

Firstly, in situ ultraviolet-visible (UV-vis) measurements were carried out during subsequent annealing at 100 °C (**Fig. 1a-1c** and **Fig. S1**). Upon thermal annealing, the absorption edge gradually shifts from ~550 nm to 800 nm, then stays mostly unchanged. For a better quantitative analysis of this annealing process, the absorbance at 460, 550, and 700 nm versus time is plotted in **Fig. 1d**. It clearly indicates two different stages, i.e, the continuous increase on the absorbance and the final stabilized state. The first (intermediate) stage corresponds to the nucleation and crystal growth processes of the precursor film, due to the increased concentration above saturation. The second stage (solid) is ascribed to the completely formed black perovskite film [26]. The time period during which the UV absorption undergoes a change from the initial point to the end is commonly known as the “crystallization window”. In this work, it specifically denotes the duration of the first stage. To quantify the crystallization difference among three films with different additives, the absorption intensity at the wavelength of 550 nm is further extracted as a function of annealing time in **Fig. 1e**. The control sample, crystallized from a disordered sol-gel, exhibits a rapid and significant increase in absorption intensity that reaches a peak at 20 seconds with no subsequent noticeable changes, indicating a narrow crystallization window of just 20 seconds (**Fig. 1f**) [27]. However, from the point of view of perovskite growth kinetics, rapid crystallization generally leads to perovskite films with low crystallinity and high defect density. Therefore, the addition of additives is necessary to regulate the crystallization process in antisolvent-free systems. For the films with additives, the evolution of the absorbance edges becomes more gradual from adding unitary additive to binary additives. This slower shift attributes to a possibly more controlled and more homogeneous crystal growth [28]. Dynamic light scattering (DLS) measurements were carried out to analyze the origin behind the crystallization difference (**Fig. S2**) [29]. The DLS results show that the average colloid sizes between the control solution and the solution with both MACl and TFAA are approximately 307 and 640 nm, respectively. Meanwhile, the Pb-I cluster size decreases for facilitating the uniform incorporation of FAI into the Pb-I framework during the nucleation and crystal growth process [30]. Moreover, the presence of a certain amount of large-sized colloids or pre-nucleated perovskite species in the precursor ink contributes to an oversaturated state of the precursor solution, leading to a faster nucleation rate and thus enabling earlier absorption changes. In this scenario, the effective mass of the solute is consumed to a large extent, which in turn delays the initiation of the crystallization process and allows ample time for crystal growth and subsequent evolution [31]. As a result, the target film exhibits the longest crystallization window about 40 s. These results are consistent with the notion that the binary additives allow longer time for perovskite nucleation and crystallization during the deposition.

The evolution of the film during annealing can be explained by the LaMer mechanism, which typically divided into three different stages of region I, II, and III, representing prenucleation, nucleation and fast-growth, as well as slow-growth and ripening, respectively, corresponding to in-situ UV–vis absorption spectra (**Fig. 1g-1i**) [32]. There is a noticeable nucleation occurring from region I to region II because the elevated substrate temperature promotes solvent evaporation and increases the precursor solution concentration until reaching the critical saturation point for nucleation ($C_c$). The reason why this stage is not observed by in situ UV-vis absorption (zero absorption change) is because the solvent can easily be self-dried during the annealing process, inducing a rapid nucleation. At region II, the solution concentration is closely related to the nucleation and growth rate. The balance of the nucleation and growth rate at this stage can effectively improve the film coverage [33]. **Fig. S3-S4** show the evolution of nuclei after the addition of additives. The precursor film of the control sample stays in region II for a long time, while the addition of binary additives generates high-density homogeneous nuclei in less than 10 s. The concentration of the complex intermediates rapidly increases and remains above $C_c$ due to the strong interactions between additives and perovskite, triggering the fast nucleation of intermediate phases. This change indicates the suppression of nucleation barrier. The energy barrier for the LaMer nucleation is related to the Gibbs free energy change of non-classical nucleation ($\Delta G^{NCN}$). According to the established nucleation theory, $\Delta G^{NCN}$ can be expressed as [34]:

$$\Delta G^{NCN} = f(\theta)\Delta G^{CN}, f(\theta) = \frac{2 - 3cos\theta + \cos^3\theta}{4} (1)$$

Equations (1) indicates that the smaller contact angle ($\theta$) results in the lower energy barrier $\Delta G^{NCN}$ [35]. As shown in **Fig. S5**, the addition of binary additives decreases the nucleation barrier for the perovskite precursor, implying that crystallization assisted by additives is more consistent with the large-grain kinetic trend. The apparent evolution of the wet film from the aforementioned process was monitored by optical microscope (**Fig. S6**). With the introduction of binary additives, the wet film shows a much longer evolution time and more stable evolution process than the control films. This observation indicates that quick oversaturation nucleation and delayed growth processes can be achieved by introducing MACl and TFAA. This capability is not inherent in common antisolvent-free methods without additives. Optical microscopy was used to track and further verify the absorption changes in the perovskite films as shown in **Fig. 1e** [36].

### *2.2. Ostwald Ripening Process, Strain Release and Passivation*

The corresponding parts to the three evolution stages can also be observed by optical microscope images, as shown in **Fig. S6**: From region I to region II, the fluid colloidal clusters nucleate into gel intermediates; at region II, the gel wet film is more likely to form islands in combination with the diffusion-nuclei; and as region III undergoes further annealing, the distance between the islands gradually decreases and merges into a large island or forms a continuous film [38]. Referring back to the previous section, the sum of regions II and III corresponds to the crystallization window. It can be clearly seen that the film with additives achieves a compact morphology without pinholes, and with large-size grains and high crystallinity (**Fig. S7-S8**). In sharp contrast, the control perovskite film displays small-size grains and obvious pinholes. It is precisely because of the rapid crystallization in conventional antisolvent-free methods. This suggests that the introduction of binary additives can easily induce the formation of compact films after the ripening process in region III. SEM images (**Fig. 2a**) shows that the average size of the grains produced in the film increases with the addition of additives, suggesting small grains merge into larger grains during film annealing process, forming a much smoother and denser film. It is consistent with the typical Ostwald ripening process, indicating that binary additives widen the crystallization window and leave sufficient time for the subsequent process [39]. The common Ostwald ripening strategies involve anion exchange at suitable concentration [40] or the addition of small molecules to disperse smaller perovskite particles and adhere to larger ones through chemical bonding [41]. This aligns precisely with the characteristics of the binary additives-MACl and TFAA. The schematic diagrams of the Ostwald ripening for both additives and their corresponding evolution processes are depicted in **Fig. S9**. MACl achieves the dissolution of smaller grains with higher surface energy and promotes the formation of larger grains with lower surface energy by participating in Cl/I anion exchange reactions with $FAPbI_3$. On the other hand, TFAA attaches to larger grains through its $–NH_3$ and –C=O groups, slowing down the diffusion and fusion of large particles. As the additives gradually volatilize, they form a continuous film. It is also the reason behind the broadening of the crystallization window. These observations hint at the synergistic effects of binary additives.

It is speculated that the ripening process can also release residual strain, which ultimately helps improve the device performance. To investigate the effects of additives on residual lattice strain ($\varepsilon$), X-ray diffraction (XRD) of annealed films were recorded. In the XRD patterns, the peak position of the (110) plane shifts from $13.97^{o}$ to $14.03^{o}$ with increasing amount of MACl (**Fig. S10**). Although the MACl generally enlarges the grain size, here it rather shifts to higher angle due to the residual compressive strain of the thin film. This can be attributed to the lattice shrink induced by strong dipolar effect of MACl, introducing compressive strain. On the contrary, the peak position of the (110) plane gradually shifts to lower angle as TFAA amount increases. The Williamson-Hall (W-H) equation is employed to estimate $\varepsilon$ using the aforementioned XRD results, through the slope of the fitting line [42]. As illustrated in **Fig. S11-S12**, the perovskite film with MACl&TFAA additives (Target) showed the lowest value of the calculated strain $1.09\times10^{-3}$, when compared to the film with MACl additive of $1.50\times10^{-3}$, indicating the release of residual strain of perovskite-substrate interfaces by the crystallization dynamics of binary additives [43]. It can be concluded that the film with MACl&TFAA exhibited smaller compressive strain in the out-of-plane orientation than the film with only MACl. To directly characterize the overall strain in more details, grazing-incidence wide-angle X-ray scattering (GIWAXS) measurements were also conducted [44]. As shown in **Fig. 2b-2d**, the scattering of TFAA&MACl film has a bit stronger intensity than the control film, especially evident with the (200) peak. These results indicate the incorporation of a small amount of additives will not change the preferred crystalline orientations, which is consistent with the results from XRD characterizations. As shown **Fig. 2e-2g**, the in-plane ($q_{xy}$) and out-of-pane ($q_z$) diffraction peaks of (110) plane are further extracted. The (110) peak in the film with binary additives has shifted to lower angles in both in-plane and out-of-plane orientations, which has happened in opposite side of the film with MACl. According to Bragg's law ($q = 2\pi/d$), the calculated interplane spacing of the (110) plane of the target film is 0.619 nm in the in-plane orientation and 0.617 nm in the out-of-plane orientation, while that of the film with MACl is 0.615 nm in the in-plane orientation and 0.615 nm in the out-of-plane orientation [37]. As demonstrated in **Fig. 2h**, within the target film, the compressive strain turns to strain-free state, and the obvious expansion in the overall orientation indicates efficiently released overall compressive strain. This also elucidates why binary additives are preferred over unitary additive.

With the step-by-step addition of additives, the XRD peak intensity of the (110) plane significantly increased and the full width at half maximum (FWHM) of GIWAXS decreased in each step (**Fig. S13-14**). With the evident changes in the perovskite (110) peak, the peak of $PbI_2$ exhibits a decrease in intensity. The thin films contain $PbI_2$ owing to anion exchange between perovskite and $PbCl_2$, resulting in an excess of $PbI_2$ in the surface, as $PbI_2$ flakes shown in **Fig. 2a**. The addition of binary additives weakens the $PbI_2$ peak, but compared to adding MACl, the binary additives slightly strengthen the peak. Previous studies have demonstrated that excessive lead iodide on the surface has a certain passivation effect [45]. To analyze the impact of $PbI_2$, the ratios of $PbI_2$ relative to $\alpha$-phase perovskite (110) are semi-empirically calculated by means of Gaussian fitting (**Fig. S14-S15**). At an increased incident angle of 0.4 to 1.0°, deeper in the bulk, the ratio of $PbI_2$ to perovskite in the control film is higher than that of the target film. This indicates that there is higher level of $PbI_2$ accumulation on the perovskite surface and is strongly suppressed in the bulk due to the additives passivation at grain boundaries (GBs) during ripening process. This also explains why binary additives can continue to enhance device performance even after volatilization. Part of the reason is their role in modulating the distribution of $PbI_2$.

### *2.3. Interactions among Additives, Perovskite and NMP*

In order to track how MACl&TFAA act and affect the crystallization process, XRD characterization was performed to probe the phase change during the annealing process, as show in **Fig. 3a-3c** and **Fig. S16**. The two peaks at 8.6° and 9.1° are attributed to the $PbI_2$•NMP adducts phase, which will dominate the nucleation [46]. As proposed, the FAI species are homogeneously distributed in the $PbI_2$•NMP adducts for in-situ forming $\alpha$-$FAPbI_3$ perovskites. For the control films, the obvious diffraction peaks corresponding to $\delta$-phase can be observed, which almost remained constant and gradually strengthen with ulteriorly increase of annealing. Hence, the control film shows small size grains and conspicuous pinholes. This represents a drawback of the general anisolvent-free method. In contrast, the addition of MACl results in a perovskite film with a smooth surface, where the previously observed holes and $\delta$-phases are eliminated. Due to the MACl-induced LaMer nucleation, substitution of the FA cation site with MACl induces an intermediate phase to the pure $\alpha$-phase and stabilizes the structure effectively without annealing. A new diffraction peak appears at 9.3°, which is demonstrate as a mixed MACl-complex intermediate [39]. MACl facilitates the transformation of the metastable nuclei by concatenation of sol clusters leading to the formation of solvent complexes, including $PbI_2$•NMP adduct and MACl-complex intermediate [47]. This is the rationale for that the peaks of solvent complexes are much stronger than the control film. As the temperature increases, a second transformation process of the solvent complexes to $FAPbI_3$ is initiated, by evaporation of the solvent from the thin film. while simultaneously the solvents and MACl are volatilized, as confirmed by the thermogravimetry-mass spectra (TG-MS) and FTIR measurements [12] (**Fig. S17-S18**). Following the introduction of TFAA to the perovskite solution, the intensity of the solvent-complex peaks intensity further increases, with the accelerated transformation to nuclei (**Fig. S16f**). At the same time, the crystallization process slows down, and the crystallinity slowly increases, resulting in stronger $\alpha$-phase peaks of the thin film finally. This can also be observed from thermogravimetry curve (**Fig. S17e**).

The function of TFAA is elucidated through further investigations. As in **Fig. S19-S20**, TFAA has a large dipole moment, and dissolving TFAA in perovskite precursor solution results in pale yellow precipitates. This implies that TFAA has a much stronger interaction with perovskite precursor [48]. To further reveal the synergy between the functional groups in TFAA and perovskite, the attenuated total internal reflectance Fourier-transform infrared (ATR-FTIR) and NMR spectroscopy are carried out. In **Fig. S21**, the hydrogen bonding between N-H unit and iodine shifts to higher wavenumber. However, the stretching vibration peak of C=O weakens and shifts to lower wavenumber, suggesting the interaction of $-C{=}O\cdots Pb$, similar to $PbI_2$•NMP bonding mode. There is also a strong interaction between FAI protons and TFAA additive, as two additional new peaks and splitting phenomenon shown in $^{1}H$ NMR spectra when adding TFAA with FAI (**Fig. 3d**) [49]. Not only $^{1}H-^{1}H$ coupling, but the fluorine on TFAA can also bond with FAI, and thus the fluorine peak in TFAA shifts toward lower ppm under the condition of blending with FAI in solution in $^{19}F$ NMR spectra (**Fig. 3f)**. Through the above analysis, the multifunctional groups in TFAA can effectively interact with perovskite fragments to achieve passivation, promoting the crystallization and stability of perovskite.

However, NMP also has a similar bonding mode, which results in a competitive relationship between TFAA and NMP, forming a complex hydrogen bonding network among FAI, TFAA, and NMP (**Fig. S22-S23**). To delineate the competition mechanism, Raman spectroscopy were carried out to reveal the coordination interaction as shown in **Fig. 3g** [50]. The strong Pb–O coordination bond in $PbI_2$•NMP adduct is identified at 147 $cm^{-1}$. The addition of TFAA results in the reduction of the Pb–O peak and the similar Pb–I vibration to $PbI_2$. Even when FAI is introduced into $PbI_2$•NMP to simulate the actual scenario, the behavior remains unchanged. In **Fig. 3i**, the TFAA additives are blended with ($PbI_2$•NMP+FAI), the C=O stretching vibration of NMP disappears and the bending vibration of $FA^+$ reappears, suggesting that TFAA promotes the formation of $FAPbI_3$ and leads to the vanishing of $PbI_2$•NMP. In conclusion, TFAA can insert between $PbI_2$ and NMP, which in turn promotes the faster departure of NMP (**Fig. S24**), allowing FAI to better interact with $PbI_2$ and form $\alpha$-$FAPbI_3$ perovskite.

Moreover, the interaction effect between MACl and TFAA is also analyzed. The $^1$H NMR spectra indicate that the peak position of MACl and TFAA almost have no change when mixing the two additives (**Fig. 3e**), implying negligible interactions between MACl and TFAA (the affinity of MACl toward $PbI_2$ results from Pb···Cl) [51]. Similarly, the stretching vibrations of C=O (NMP), C=N ($FA^+$), and C–N ($MA^+$) in the **Fig. 3j** are observed. It was reported that: MACl could quickly induce nuclei to form pure $\alpha$-phase $FAPbI_3$ and dramatically reduce phase-transition temperatures [52]. Moreover, $MA^+$ is more easily incorporated into perovskite framework than $FA^+$, resulting in a lower formation energy as evidenced by the blue shift of Pb-I peak towards the perovskite Pb-I framework in **Fig. 3h** [53]. As a comparably volatile additive, though TFAA is unable to lower the formation energy, it possesses multiple functional groups that can resist $\delta$-phase formation (**Fig. S16c**) and facilitate NMP evaporation (**Fig. S17f**). Additionally, the departure of large-molecule additives can prevent the introduction of extra defects resulting from residues. Therefore, binary additives play distinct roles, with MACl reducing the formation energy and TFAA facilitating the transformation of the intermediate phase to the $\alpha$-perovskite phase.

Combining the observations discussed above, the crystallization can be described by the two paths as following (**Fig. 3k**): Upon adding MACl to the precursor solution, the coordination complex ($PbI_2$·NMP)+MACl+FAI is formed. Upon introducing heat, the system, which originally forms the MACl-complex intermediates, is directly converted into $\alpha$-phase

$(FA_xMA_{1-x})Pb(I_xCl_{1-x})_3$ perovskite intermediates with the insertion of MACl. With further volatilization of NMP and MACl during the ripening process, the $\alpha$-phase perovskite film finally forms. TFAA follows a similar pathway. Lattice distortion is also released during the ripening process (**Fig. S25**). In-situ XRD analysis confirm that the introduction of TFAA enhances the stability of the intermediate phase and assists in suppressing uncontrolled reactions between FAI and $PbI_2$ through the similar binding mode to that of NMP. Since TFAA has a lower volatility than solvent (DMF and NMP), it escapes with MACl from solution later (**Fig. S17g**). Because the evaporation occurs at the liquid-air interface, this process leaves more stable TFAA behind at the surface of the solution. It is the process that leads to the spontaneous down-top passivation of grain boundaries by MACl&TFAA. As heat is continuously supplied and the temperature rises to a high-boiling-point, the coordinating TFAA also evaporates, leading to the eventual formation of the $FAPbI_3$ phase (**Fig. S17d** and **Fig. S18**). This entire process can be summarized in the following pathway:

$$\text{TFAA-}(PbI_2 \bullet \text{NMP}) + \text{MACl} + \text{FAI} \xrightarrow[\Delta]{\text{NMP}\uparrow} \text{TFAA-}(FA_xMA_{1-x})Pb(I_xCl_{1-x})_3 \xrightarrow[\Delta]{\text{MACl, TFAA}\uparrow} FAPbI_3 \quad (2)$$

In summary, in a one-step process without antisolvent system, the intermediate phases modulated by additives can regulate the crystallization process, enhance the crystallinity of perovskite thin films, and ultimately yield uniform perovskite thin films, thus rivaling systems that incorporate with antisolvent (**Table S1**).

To gain a more profound insight into the role of the unique additive-TFAA, density functional theory (DFT) calculations [54] were performed to quantify the interaction energies between small molecules (TFAA and NMP) and the perovskite species (FAI and $PbI_2$), as summaried in **Fig. 4a-4b** and **Table S2**. However, in terms of bimolecular interactions, the interaction energies between NMP and the perovskite species are stronger than those between TFAA and the perovskite species, indicating the higher stabilization caused by NMP. Nevertheless, in the case of trimolecular interactions, the introduction of passivating agent (TFAA) increases precursor stability, as the interaction energies between $PbI_2$·NMP/FAI·NMP and TFAA are lower than those with NMP alone. These results are consistent with NMR analysis and FTIR measurements, further confirming that no matter how NMP is combined with $PbI_2$/FAI, in the presence of TFAA, the TFAA complex ($PbI_2$·TFAA·FAI) is partially formed with energy close to that of FAI·NMP·$PbI_2$ (**Fig. 4c**). As expected, TFAA has a similar bonding mode to NMP, allowing it to partially replace NMP in the perovskite system, thereby accelerating the formation of the perovskite phase (**Fig. S26**).

This finding aligns with the previous discussion regarding the ability of TFAA to insert between $PbI_2$ and NMP, facilitating the accelerated departure of NMP (**Fig. 4d**). Furthermore, the molecular configuration $PbI_2$·TFAA·NMP is validated through computational simulations **(Fig. S27-S28)**. The underlying mechanism for the enlarged crystallization window without antisolvent in TFAA-incorporated perovskite films can be attributed to the interactions between TFAA and precursors. Two different intermediate transformation processes drive the generation of more prenucleation sites, and TFAA around these nuclei also slows down their growth and fusion. Furthermore, hydrogen bonding also slow down crystallization [55]. Therefore, the addition of TFAA can enhance the quality of perovskite films. Although the intermediate phases simulated by DFT are not stable and difficult to characterize (**Fig. S29**), the intermediate phases themselves, as transitional points for perovskite phase transformation, serve to bridge the thermodynamic energy and kinetic pathways. The rapid transformation of the intermediate phases also indicates that their modulating role is conducive to nucleation and crystallization. Additionally, this “binary volatile additive” strategy exhibits lower-FA content applicability (**Fig. S30**).

### *2.4. The Influence of Binary Volatile Additives on the Perovskite Film Characteristic and Photovoltaic Performance*

One of the important questions related to the role of binary additives is how they enhance the performance of the perovskite film, considering both TFAA and MACl are volatile additives. As is confirmed by X-ray photoelectron spectroscopy (XPS) [56], the additive-treatment of perovskite films passivates grain boundaries and manipulates composition stoichiometry. In **Fig. 5a**, the Pb *4f* core levels of the target perovskite film exhibit a slight shift towards lower binding energies. This indicates a variation in the surface homogeneity, as evidenced by the decrease in $Pb^0$ signals in the target film, suggesting a reduction in halide vacancies [57]. **Fig. 5b** reveals that the control perovskite film has an iodine-rich surface condition, while the target film achieves effective iodine management, approaching a stoichiometric I/Pb ratio (**Fig. S31**). In addition, from energy-dispersive spectroscopy (EDS) mapping (**Fig. S32-34**), the improvement of composition homogeneity in target film was found. These finding correlate with the reduced occurrence of visible pinholes in the control film. In **Fig. 5c-5d**, the SEM images show that the control film has poor coverage with many visible pinholes, which are known to contribute to the formation of significant charged defects. When modifying the perovskite films by introducing binary additives, they act as seeds to improve nucleation and crystal growth, leading to the formation of dense and uniform films with larger grain sizes. Therefore, a strong correlation exists between the size of colloidal particles in the perovskite precursor and the grain size of the final perovskite polycrystalline film. Atomic force microscopy (AFM) images (**Fig. S35**) also show uniformly smooth film characteristics, particularly with controlled excess $PbI_2$ (white flakes), consistent with **Fig. S12**. However, an excess of additives is not viable in **Fig. S36**.

It is natural to associate improved homogeneity with reduced number of defects. To validate this viewpoint, the impact of additive treatment on perovskite films is investigated in terms of defect passivation observed through steady-state photoluminescence (PL) and time-resolved PL (TRPL) measurements [58] (**Fig. 5e-5f**). Compared to the control film, the treated perovskite films exhibit significantly enhanced PL intensities, with the MACl&TFAA-treated film showing the highest enhancement. Furthermore, the PL peak position for the control film, initially centered at 800 nm, shifts to 780 nm with the introduction of binary additives, indicating a reduction in defect density of the bulk. The prolonged PL lifetimes of films treated with MACl (273.86 ns) and MACl&TFAA (398.57 ns) compared to the control film (248.22 ns) further highlight the efficient passivation effect (**Table S3**). PL-mapping characterization (**Fig. 5g-5h**) confirms the enhanced PL intensity after treatment, observed in a 30μm×30μm perovskite film area.

In addition, changes in energy band levels can be observed from the ultraviolet photoelectron spectroscopy (UPS) measurements, which reveal an increased work function (WF) from 3.90 to 4.43 eV with the introduction of binary additives (**Fig. 5i**). Valence band edge measurements indicate that the perovskite films without and with additive treatment are positioned 1.34 and 0.91 eV below the Fermi level, respectively. Combining bandgap and UPS measurements, an energy-level diagram is constructed (**Fig. S37** and **Fig. 5j**). This diagram indicates a shift of the Fermi level towards the vacuum level after the binary-additives treatment, indicating that the target film has a more p-type character. Studies show that variations in the negative work function ($\Delta W$) lead to charge accumulation, reducing halide migration activation energy and compromising PSC stability [59]. UPS measurements confirm that additive-treated surfaces exhibit a positive $\Delta W$, which is consistent for both monomeric and dimeric additives. This positive $\Delta W$, associated with p-type surfaces, enhances hole transport towards the hole transport layer (HTL), improving optoelectronic performance. This result was also supported by Kelvin probe force microscopy (KPFM), as can be seen in **Fig. 5k-5l**. KPFM measurements validate the work function distribution, revealing a consistent contact potential difference change (ΔCPD) with ΔW. The relationship between ΔCPD and ΔW, as detailed below:

$$V_{CPD-additive}=W_{additive}-W_{tip},V_{CPD-Control}=W_{Control}-W_{tip}\left(3\right)$$

$$\Delta CPD=V_{CPD-additive}-V_{CPD-Control}\text{¿}W_{additive}-W_{Control}=\Delta W$$

Based on UPS and KPFM results, positive ΔW is predicted to suppress potential traps formation at surface interfaces (**Fig. S38-S39**).

The implementation of the binary volatile additive approach yields multiple beneficial alterations in perovskite films, consequently impacting the device characteristics. To investigate the influence of additives on the photovoltaic performance, antisolvent-free PSCs with an n-i-p structure of ITO/$SnO_2$/perovskite/Spiro-OMeTAD/Au were fabricated (**Fig. 6a**). Firstly, the relationship between device performance and the concentration of MACl and TFAA binary additives is investigated, as shown in **Fig. S40-S41** and **Table S4-S6** of the Supporting Information. The incorporation of MACl&TFAA yielded an all-round performance improvement for antisolvent-free PSCs, leading to an average PCE increase from 17.3% to 22.0%. The enhancement of integrated $J_{SC}$ can also serve as evidence (**Fig. S42**). For the champion device, the PCE increases to 22.4% with open-circuit voltage ($V_{OC}$) of 1.136 V, short circuit current density ($J_{SC}$) of 24.51 mA•$cm^{-2}$ and fill factor (FF) of 80.34%, which is relatively high efficiency for antisolvent-free PSCs (**Fig. 6b**). The statistics of photovoltaic parameters in **Fig. 6c** further illustrate the reproductivity of target device and the performance has been significantly improved. The improvement in PCE relies on the enhancement of electronic properties. Charge recombination kinetics within the PSCs are investigated by studying the relationships of $V_{OC}$ versus the light intensities. As shown in **Fig. 6d**, according to the fitted line, the slope of the target PSC is calculated to be 1.44 $k_BT/q$, which is smaller than 2.89 $k_BT/q$ of the control PSC. This decreased value indicates a decreased monomolecular Shockley-Read-Hall recombination process [60]. This phenomenon can also be confirmed by the space-charge-limited-current trap (SCLC) technique. SCLC was employed to measure defect density of perovskite films based on a hole-only structure of ITO/PTAA/perovskites/Spiro-OMeTAD/Au (**Fig. 6e**). The calculated defect density decreases from $6.92\times10^{15}$ to $2.98\times10^{15}$ $cm^{-3}$, indicating the reduced defects of the perovskite film with the addition of binary additives [61]. Electrochemical impedance spectroscopy (EIS) measurements illustrate smaller semicircle radius and smaller charge transport resistance ($R_{ct}$) of the target devices compared with the control (**Fig. 6f**), which indicates accelerated charge-transport across perovskite [62].

The stability of antisolvent-free PSCs devices is investigated under multi-field conditions. As shown in **Fig. 6g**, target PSCs exhibit excellent long-term shelf stability under environmental storage testing after 1092 h storage (25 °C, 35±5 % relative humidity). The ambient and thermal stability are also tested. Compared with the control device, the additives-treated device shows improved stability with a RH of 60±5 %. In particular, the target device maintains 77 % of its initial PCE after 660 h, while that of the control device degrades by 60 % during the same testing period (**Fig. S43**). The thermal stability of target devices maintains 82 % with heating at 60±3 °C in a nitrogen-filled glovebox, while the PCE of the control device is only 68 % of the initial value after 660 h of heating. The improved stability of PSC devices is attributed to the refined perovskite structure perfection with addition of binary additives, which can passivate defects and suppress ion migration (**Table S7-S8**), thereby delay device performance degradation.

## 3. Conclusion

In conclusion, this work demonstrates a facile approach of using MACl&TFAA binary volatile additives to modulate the crystallization process for obtaining high-quality pinhole-free $FA_{0.9}Cs_{0.1}Pb(I_xCl_{1-x})_3$ perovskite films. With the combination of experimental and theoretical analysis, we unveil the crystallization mechanism in this antisolvent-free system. ATR-FTIR, NMR, Raman spectroscopy, and DFT calculations evaluate the coordination mode among $PbI_2$ and binary additives in perovskite intermediates, establishing a link between the broadening of the macroscopic crystallization window and the microscopic molecular interaction mechanisms. The binary volatile additives play distinct roles: MACl additive reduces the formation energy required for the $\alpha$-phase perovskite, thereby promoting the formation of nuclei; TFAA additive expedites initial nucleation by replacing NMP, resulting in the broadening of the crystallization window, as evidenced by in-situ XRD and UV-vis absorption spectra. The roles of the binary volatile additives are also complementary, leading to the bottom-up passivation of grain boundaries, release of grain strain, and suppression of defect states. The synergistic effect of binary additives increases carrier extraction efficiency and maintains chemical homogeneity in the devices. As a result, antisolvent-free PSCs with binary additives achieved evidently enhanced PCE (up to 22.4%) and improved environmental stability comparing to the control devices. This work presents an effective approach to further enhance the device performance of antisolvent-free PSCs with excellent reproducibility and explores the synergistic effects of binary additives. Moreover, this strategy can be potentially applied in industrially compatible coating techniques for the fabrication of commercialized perovskite products.

## Declaration of Competing Interest

The authors declare that they have no known competing financial interests or personal relationships that could have appeared to influence the work reported in this paper.

## Acknowledgements

The work was also performed by the Fundamental Research Center of Artificial Photosynthesis (FReCAP), supported through National Natural Science Foundation of China (22088102). P. Zhao would like to thank Prof. M. Ehara for the support of computational resources in Research Centre for Computational Science, Okazaki, Japan (Project: 22-IMS-C185).

## Appendix A. Supporting information

Supplementary data associated with this article can be found in the online version.

## References

[1] NREL, National Renewable Energy Laboratory Best Research Cell Efficiency Chart, https://www.nrel.gov/pv/cell-efficiency.html (accessed August 2023).

[2] Y. Huang, X. Lei, T. He, Y. Jiang, M. Yuan, Adv. Energy Mater. 12 (2022) 2100690, https://doi.org/10.1002/aenm.202100690.

[3] T. Bu, X. Liu, J. Li, W. Huang, Z. Wu, F. Huang, Y.-B. Cheng, J. Zhong, Sol. RRL 4 (2020) 1900263, https://doi.org/10.1002/solr.201900263.

[4] Y. Sun, Q. Yao, W. Xing, H. Jiang, Y. Li, W. Xiong, W. Zhu, Y. Zheng, Adv. Sci. (2022) 2205986, https://doi.org/10.1002/advs.202205986.

[5] W. Xu, Y. Gao, W. Ming, F. He, J. Li, X.-H. Zhu, F. Kang, J. Li, G. Wei, Adv. Mater. 32 (2020) 2003965, https://doi.org/10.1002/adma.202003965.

[6] L. Chao, T. Niu, W. Gao, C. Ran, L. Song, Y. Chen, W. Huang, Adv. Mater. 33 (2021) 2005410, https://doi.org/10.1002/adma.202005410.

[7] N.K. Noel, S.N. Habisreutinger, B. Wenger, M.T. Klug, M.T. Hörantner, M.B. Johnston, R.J. Nicholas, D.T. Moore, H.J. Snaith, Energy Environ. Sci. 10 (2017) 145-152, https://doi.org/10.1039/c6ee02373h.

[8] Q. Zhang, G. Ma, K.A. Green, K. Gollinger, J. Moore, T. Demeritte, P.C. Ray, G.A. Hill, Jr., X. Gu, S.E. Morgan, M. Feng, S. Banerjee, Q. Dai, ACS Appl. Energy Mater 5 (2022) 1487-1495, https://doi.org/10.1021/acsaem.1c02879.

[9] Y. Deng, C.H. Van Brackle, X. Dai, J. Zhao, B. Chen, J. Huang, Sci. Adv. 5 (2019) eaax7537, https://doi.org/10.1126/sciadv.aax7537.

[10] X. Huang, F. Cao, S. Zhan, Q. Feng, M. Zhu, Z. Su, X. Gao, J. Yin, J. Li, N. Zheng, B. Wu, Joule 7 (2023) 1-18, https://doi.org/10.1016/j.joule.2023.05.020.

[11] C. Wu, D. Wang, Y. Zhang, F. Gu, G. Liu, N. Zhu, W. Luo, D. Han, X. Guo, B. Qu, S. Wang, Z. Bian, Z. Chen, L. Xiao, Adv. Funct. Mater. 29 (2019) 1902974, https://doi.org/10.1002/adfm.201902974.

[12] J. Chung, S.-W. Kim, Y. Li, T. Mariam, X. Wang, M. Rajakaruna, M.M. Saeed, A. Abudulimu, S.S. Shin, K.N. Guye, Z. Huang, R.J.E. Westbrook, E. Miller, B. Subedi, N.J. Podraza, M.J. Heben, R.J. Ellingson, D.S. Ginger, Z. Song, Y. Yan, Adv. Energy Mater. (2023) 2300595, https://doi.org/10.1002/aenm.202300595.

[13] G. Tong, J. Zhang, T. Bu, L.K. Ono, C. Zhang, Y. Liu, C. Ding, T. Wu, S. Mariotti, S. Kazaoui, Y. Qi, Adv. Energy Mater. 13 (2023) 2300153, https://doi.org/10.1002/aenm.202300153.

[14] G. Li, Z. Wang, Y. Wang, Z. Yang, P. Dong, Y. Feng, Y. Jiang, S.-P. Feng, G. Zhou, J.-M. Liu, J. Gao, Small (2023) 2301323, https://doi.org/10.1002/smll.202301323.

[15] T. Bu, J. Li, H. Li, C. Tian, J. Su, G. Tong, L.K. Ono, C. Wang, Z. Lin, N. Chai, X.-L. Zhang, J. Chang, J. Lu, J. Zhong, W. Huang, Y. Qi, Y.-B. Cheng, F. Huang, Science 372 (2021) 1327-1332, https://doi.org/10.1126/science.abh1035.

[16] K. Odysseas Kosmatos, L. Theofylaktos, E. Giannakaki, D. Deligiannis, M. Konstantakou, T. Stergiopoulos, Energy Environ. Sci. 2 (2019) 79-92, https://doi.org/10.1002/eem2.12040.

[17] L. Bi, Q. Fu, Z. Zeng, Y. Wang, F.R. Lin, Y. Cheng, H.-L. Yip, S.W. Tsang, A.K.Y. Jen, J. Am. Chem. Soc. 145 (2023) 5920-5929, https://doi.org/10.1021/jacs.2c13566.

[18] M. Kim, G.-H. Kim, T.K. Lee, I.W. Choi, H.W. Choi, Y. Jo, Y.J. Yoon, J.W. Kim, J. Lee, D. Huh, H. Lee, S.K. Kwak, J.Y. Kim, D.S. Kim, Joule 3 (2019) 2179-2192, https://doi.org/10.1016/j.joule.2019.06.014.

[19] D. Wang, J. Chen, P. Zhu, Y. Qiao, H. Hu, J. Zeng, J. Zhang, G. Qu, Y. Wang, X. Wang, A.K.-Y. Jen, B. Xu, Adv. Energy Mater. 13 (2023) 2203649, https://doi.org/10.1002/aenm.202203649.

[20] Q. Yang, X. Liu, S. Yu, Z. Feng, L. Liang, W. Qin, Y. Wang, X. Hu, S. Chen, Z. Feng, G. Hou, K. Wu, X. Guo, C. Li, Energy Environ. Sci. 14 (2021) 6536-6545, https://doi.org/10.1039/d1ee02248b.

[21] L. Liu, Y. Li, C. Zheng, Z. Liu, N. Yuan, J. Ding, D. Wang, S. Liu, Sol. RRL 6 (2022) 2200284, https://doi.org/10.1002/solr.202200284.

[22] P. Li, H. Dong, J. Li, X. Cao, J. Xi, D. Wang, B. Jiao, X. Hou, Y. Yang, Z. Wu, Org. Electron. 113 (2023) 106707, https://doi.org/10.1016/j.orgel.2022.106707.

[23] X. Jiang, G. Yang, B. Zhang, L. Wang, Y. Yin, F. Zhang, S. Yu, S. Liu, H. Bu, Z. Zhou, L. Sun, S. Pang, X. Guo, Angew Chem Int Ed Engl (2023) e202313133, https://doi.org/10.1002/anie.202313133.

[24] Z. Lin, Y. Su, R. Dai, G. Liu, J. Yang, W. Sheng, Y. Zhong, L. Tan, Y. Chen, ACS Appl. Mater. Interfaces 13 (2021) 15420-15428, https://doi.org/10.1021/acsami.1c01408.

[25] Y. Yang, J. Wu, X. Wang, Q. Guo, X. Liu, W. Sun, Y. Wei, Y. Huang, Z. Lan, M. Huang, J. Lin, H. Chen, Z. Wei, Adv. Mater. 32 (2020) 1904347, https://doi.org/10.1002/adma.201904347.

[26] H. Hu, Z. Ren, P.W.K. Fong, M. Qin, D. Liu, D. Lei, X. Lu, G. Li, Adv. Funct. Mater. 29 (2019), https://doi.org/10.1002/adfm.201900092.

[27] Y. Zhang, J. Wen, Z. Xu, D. Liu, T. Yang, T. Niu, T. Luo, J. Lu, J. Fang, X. Chang, S. Jin, K. Zhao, S. Liu, Adv. Sci. 8 (2021) 2001433, https://doi.org/10.1002/advs.202001433.

[28] M.M. Byranvand, T. Kodalle, W. Zuo, T. Magorian Friedlmeier, M. Abdelsamie, K. Hong, W. Zia, S. Perween, O. Clemens, C.M. Sutter-Fella, M. Saliba, Adv. Sci. 9 (2022) 2202441, https://doi.org/10.1002/advs.202202441.

[29] B. Li, M. Li, C. Fei, G. Cao, J. Tian, J. Mater. Chem. A 5 (2017) 24168-24177, https://doi.org/10.1039/C7TA08761F.

[30] Y. Wu, G. Xu, J. Xi, Y. Shen, X. Wu, X. Tang, J. Ding, H. Yang, Q. Cheng, Z. Chen, Y. Li, Y. Li, Joule 7 (2023) 398-415, https://doi.org/10.1016/j.joule.2022.12.013.

[31] W. Feng, J. Tao, G. Liu, G. Yang, J.-X. Zhong, Y. Fang, L. Gong, S. Yang, W.-Q. Wu, Angew Chem Int Ed Engl 62 (2023) e202300265, https://doi.org/10.1002/anie.202300265.

[32] M. Jung, S.-G. Ji, G. Kim, S.I. Seok, Chem. Soc. Rev. 48 (2019) 2011-2038, https://doi.org/10.1039/C8CS00656C.

[33] L. Zeng, S. Chen, K. Forberich, C.J. Brabec, Y. Mai, F. Guo, Energy Environ. Sci. 13 (2020) 4666-4690, https://doi.org/10.1039/D0EE02575E.

[34] W. Chen, Y. Huang, H. Cui, S. Li, Y. Feng, B. Zhang, Small Methods 7 (2023) 2201276, https://doi.org/10.1002/smtd.202201276.

[35] J.W. Yoo, J. Jang, U. Kim, Y. Lee, S.-G. Ji, E. Noh, S. Hong, M. Choi, S.I. Seok, Joule 5 (2021) 2420-2436, https://doi.org/10.1016/j.joule.2021.08.005.

[36] Z. Yang, W. Zhang, S. Wu, H. Zhu, Z. Liu, Z. Liu, Z. Jiang, R. Chen, J. Zhou, Q. Lu, Z. Xiao, L. Shi, H. Chen, L.K. Ono, S. Zhang, Y. Zhang, Y. Qi, L. Han, W. Chen, Sci. Adv. 7 (2021) eabg3749, https://doi.org/10.1126/sciadv.abg3749.

[37] L. Deng, X. Li, S. Rafique, Y. Wang, Y. Wang, K. Liu, F. Liu, Y. Pan, X. Yue, J. Wang, J. Tang, Y. Yang, H. Wang, Z. Shi, C. Li, Y. Qin, A. Yu, Y. Zhan, ACS Appl. Mater. Interfaces 14 (2022) 52007-52016, https://doi.org/10.1021/acsami.2c16247.

[38] K. Liao, C. Li, L. Xie, Y. Yuan, S. Wang, Z. Cao, L. Ding, F. Hao, Nano-micro Lett 12 (2020) 156, https://doi.org/10.1007/s40820-020-00494-2.

[39] T. Bu, L.K. Ono, J. Li, J. Su, G. Tong, W. Zhang, Y. Liu, J. Zhang, J. Chang, S. Kazaoui, F. Huang, Y.-B. Cheng, Y. Qi, Nat. Energy 7 (2022) 528-536, https://doi.org/10.1038/s41560-022-01039-0.

[40] M. Yang, T. Zhang, P. Schulz, Z. Li, G. Li, D.H. Kim, N. Guo, J.J. Berry, K. Zhu, Y. Zhao, Nat. Commun. 7 (2016) 12305, https://doi.org/10.1038/ncomms12305.

[41] N.D. Pham, V.T. Tiong, D. Yao, W. Martens, A. Guerrero, J. Bisquert, H. Wang, Nano Energy 41 (2017) 476-487, https://doi.org/10.1016/j.nanoen.2017.10.006.

[42] H. Min, S.-G. Ji, S.I. Seok, Joule 6 (2022) 2175-2185, https://doi.org/10.1016/j.joule.2022.06.031.

[43] W. Lv, Z. Hu, W. Qiu, D. Yan, M. Li, A. Mei, L. Xu, R. Chen, Adv. Sci. 9 (2022) 2202028, https://doi.org/10.1002/advs.202202028.

[44] B. Yang, D. Bogachuk, J. Suo, L. Wagner, H. Kim, J. Lim, A. Hinsch, G. Boschloo, M.K. Nazeeruddin, A. Hagfeldt, Chem. Soc. Rev. 51 (2022) 7509-7530, https://doi.org/10.1039/D2CS00278G.

[45] X. Jiang, J. Zhang, X. Liu, Z. Wang, X. Guo, C. Li, Angew Chem Int Ed Engl 61 (2022) e202115663, https://doi.org/10.1002/anie.202115663.

[46] X. Zhang, X. Li, L. Tao, Z. Zhang, H. Ling, X. Fu, S. Wang, M.J. Ko, J. Luo, J. Chen, Y. Li, Small 2208289, https://doi.org/10.1002/smll.202208289.

[47] S. Pratap, F. Babbe, N.S. Barchi, Z. Yuan, T. Luong, Z. Haber, T.-B. Song, J.L. Slack, C.V. Stan, N. Tamura, C.M. Sutter-Fella, P. Müller-Buschbaum, Nat. Commun. 12 (2021) 5624, https://doi.org/10.1038/s41467-021-25898-5.

[48] X. Jiang, B. Zhang, G. Yang, Z. Zhou, X. Guo, F. Zhang, S. Yu, S. Liu, S. Pang, Angew Chem Int Ed Engl 62 (2023) e202302462, https://doi.org/10.1002/anie.202302462.

[49] W.T.M. Van Gompel, R. Herckens, G. Reekmans, B. Ruttens, J. D'Haen, P. Adriaensens, L. Lutsen, D. Vanderzande, J. Phys. Chem. C 122 (2018) 4117-4124, https://doi.org/10.1021/acs.jpcc.7b09805.

[50] X. Huang, G. Deng, S. Zhan, F. Cao, F. Cheng, J. Yin, J. Li, B. Wu, N. Zheng, ACS Cent. Sci. 8 (2022) 1008-1016, https://doi.org/10.1021/acscentsci.2c00385.

[51] L.E. Lehner, S. Demchyshyn, K. Frank, A. Minenkov, D.J. Kubicki, H. Sun, B. Hailegnaw, C. Putz, F. Mayr, M. Cobet, G. Hesser, W. Schöfberger, N.S. Sariciftci, M.C. Scharber, B. Nickel, M. Kaltenbrunner, Adv. Mater. 35 (2023) 2208061, https://doi.org/10.1002/adma.202208061.

[52] F. Ye, J. Ma, C. Chen, H. Wang, Y. Xu, S. Zhang, T. Wang, C. Tao, G. Fang, Adv. Mater. 33 (2021) 2007126, https://doi.org/10.1002/adma.202007126.

[53] J.A. Steele, H. Yuan, C.Y.X. Tan, M. Keshavarz, C. Steuwe, M.B.J. Roeffaers, J. Hofkens, ACS nano 11 (2017) 8072-8083, https://doi.org/10.1021/acsnano.7b02777.

[54] J.-W. Lee, Z. Dai, C. Lee, H.M. Lee, T.-H. Han, N. De Marco, O. Lin, C.S. Choi, B. Dunn, J. Koh, D. Di Carlo, J.H. Ko, H.D. Maynard, Y. Yang, J. Am. Chem. Soc. 140 (2018) 6317-6324, https://doi.org/10.1021/jacs.8b01037.

[55] H.-H. Huang, Q.-H. Liu, H. Tsai, S. Shrestha, L.-Y. Su, P.-T. Chen, Y.-T. Chen, T.-A. Yang, H. Lu, C.-H. Chuang, K.-F. Lin, S.-P. Rwei, W. Nie, L. Wang, Joule 5 (2021) 958-974, https://doi.org/10.1016/j.joule.2021.02.012.

[56] K. Xie, X. Liu, H. Li, L. Fang, K. Xia, D. Yang, Y. Zou, X. Zhang, Carbon Energy (2023) e427, https://doi.org/10.1002/cey2.427.

[57] L. Yuan, J. Wang, P. Huang, Q. Yin, S. Zou, L. Wang, Z. Zhang, H. Luo, F. Liu, J. Qiu, J. Xie, L. Ding, K. Yan, Small Methods 7 (2023) 2201467, https://doi.org/10.1002/smtd.202201467.

[58] Y. Li, H. Fan, F. Xu, T. Wang, C. Shan, W. Li, X. Gu, X. Lai, D. Luo, Z. Sun, M. Zhao, X. Li, K. Cui, G. Li, A.K.K. Kyaw, Sol. RRL 6 (2022) 2200816, https://doi.org/10.1002/solr.202200816.

[59] S. Tan, T. Huang, I. Yavuz, R. Wang, T.W. Yoon, M. Xu, Q. Xing, K. Park, D.-K. Lee, C.-H. Chen, R. Zheng, T. Yoon, Y. Zhao, H.-C. Wang, D. Meng, J. Xue, Y.J. Song, X. Pan, N.-G. Park, J.-W. Lee, Y. Yang, Nature 605 (2022) 268–273, https://doi.org/10.1038/s41586-022-04604-5.

[60] Z. Wang, L. Liu, X. Liu, D. Song, D. Shi, S. Wu, Y. Tong, H. Ren, M. Li, Y. Zheng, D. Zhao, Chem. Eng. J. 432 (2022) 134367, https://doi.org/10.1016/j.cej.2021.134367.

[61] W. Nie, H. Tsai, R. Asadpour, J.C. Blancon, A.J. Neukirch, G. Gupta, J.J. Crochet, M. Chhowalla, S. Tretiak, M.A. Alam, H.L. Wang, A.D. Mohite, Science 347 (2015) 522-525, https://doi.org/10.1126/science.aaa0472.

[62] Y. Zhao, P. Zhu, S. Huang, S. Tan, M. Wang, R. Wang, J. Xue, T.-H. Han, S.-J. Lee, A. Zhang, T. Huang, P. Cheng, D. Meng, J.-W. Lee, J. Marian, J. Zhu, Y. Yang, J. Am. Chem. Soc. 142 (2020) 20071-20079, https://doi.org/10.1021/jacs.0c09560.

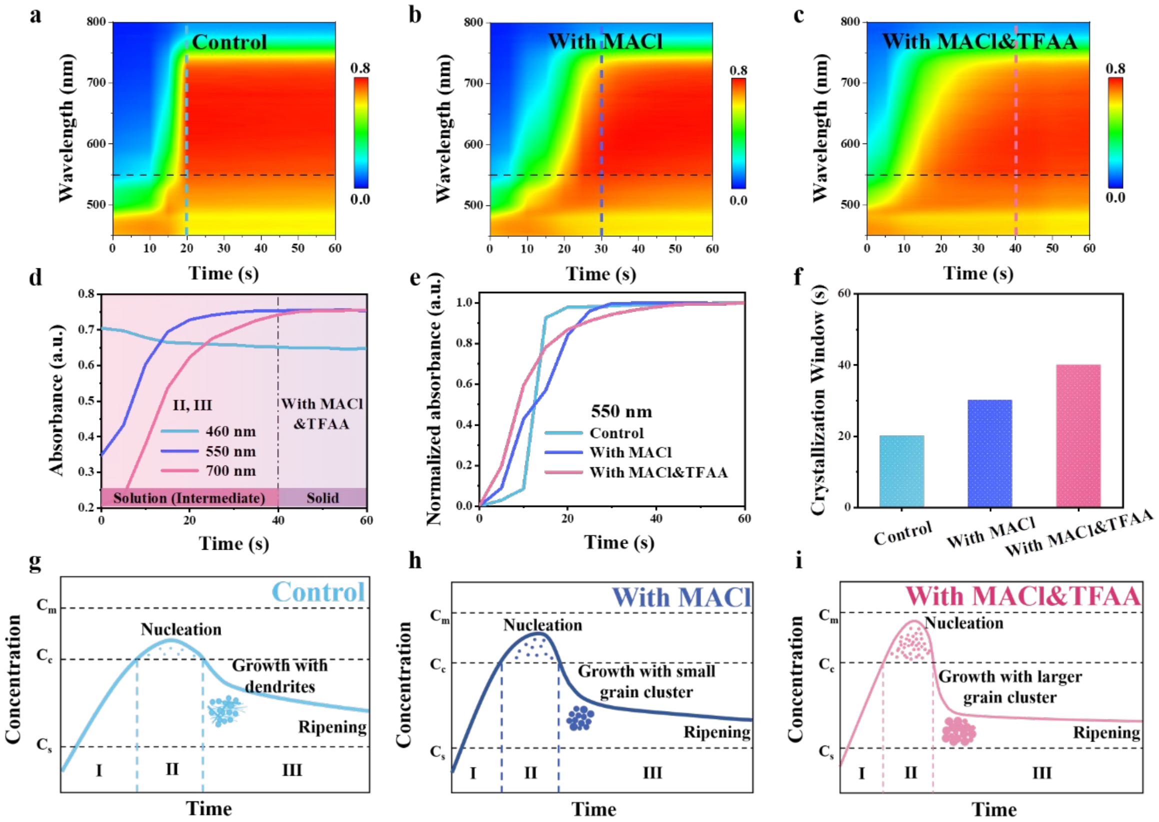

**Fig. 1.** Crystal growth of perovskite films. In situ UV-vis absorption spectra of perovskite films for spin-coating (10 s) with different conditions: a) Control, b) with MACl, and c) with MACl&TFAA. d) Time-resolved absorbance at the wavelength of 460, 550 and 700 nm,

respectively [26]. e) UV-Vis absorption of different perovskite films extracted at the wavelength of 550 nm as a function of thermal annealing time. f) Crystallization window without and with different additives. g-i) Schematic illustration of nucleation and growth process based on the LaMer mechanism.

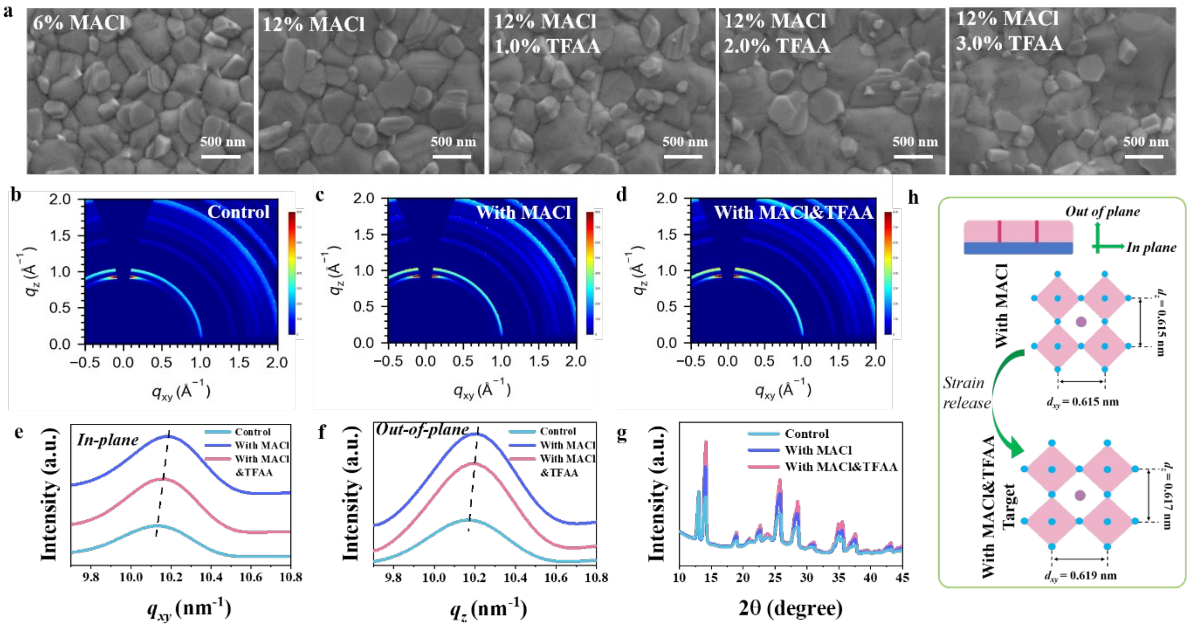

**Fig. 2.** Correlation between Ostwald ripening and micro strain with conditions. a) SEM surface images of thin films with different amounts of additives. b-d) 2D GIWAXS diffraction patterns for the three films with different conditions, and e-g) 1D GIWAXS patterns for the same films in the in-plane, out-of-plane orientation, and all orientation respectively. h) Unit cell diagram of the perovskites films with MACl and the target film [4, 37].

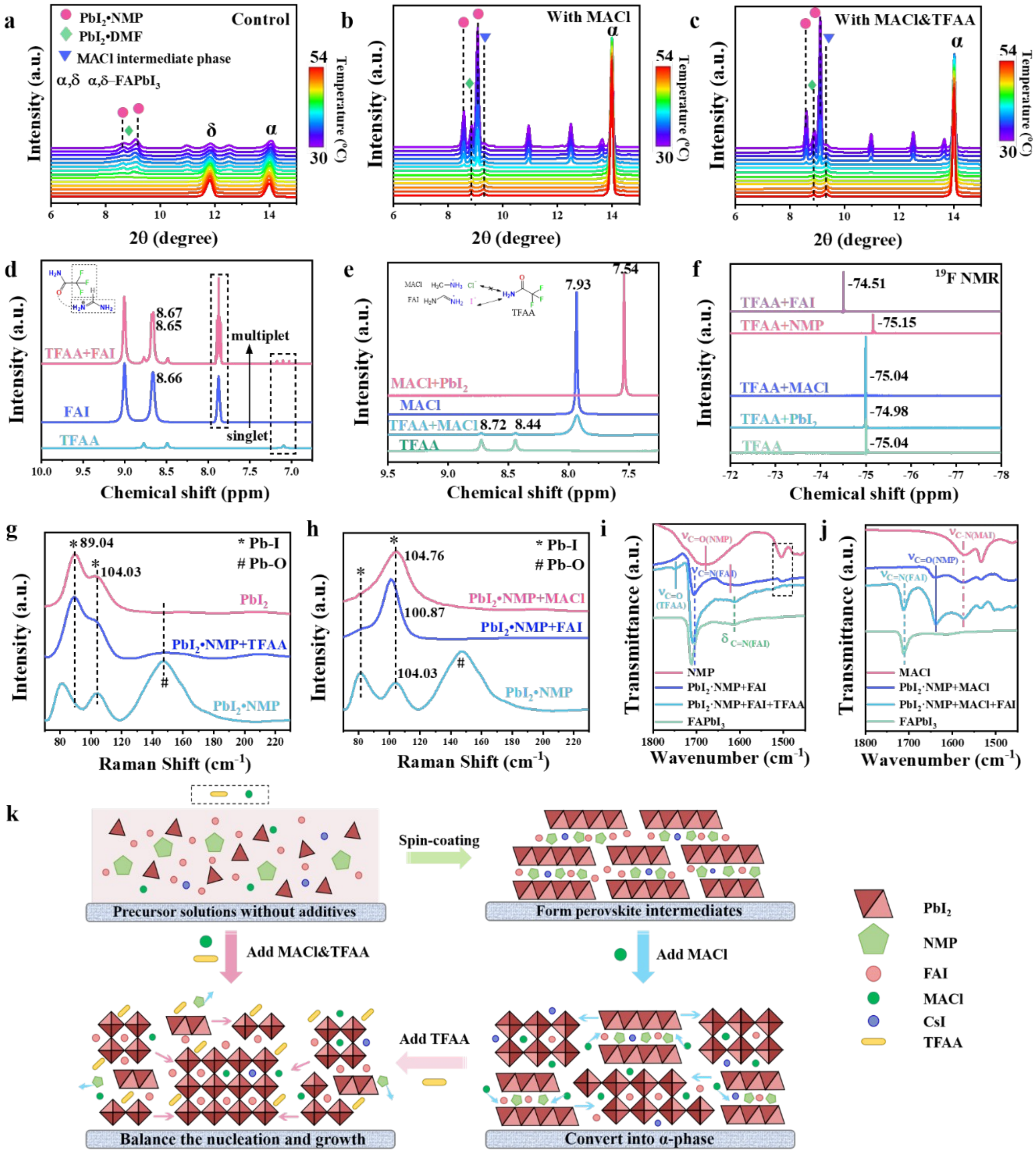

**Fig. 3.** Characterization of molecular interactions. a-c) In-situ XRD patterns of perovskite films without or with additives annealed at different temperatures. d) $^1$H NMR spectra of the interaction between TFAA and FAI, with the block showing the splitting phenomenon. e) $^1$H NMR spectra illustrates that TFAA and MACl are not mutually interferential. f) $^{19}$F NMR spectra shows the interactions of TFAA with other molecules. g-h) Demonstration of the Pb–O and Pb-I bond within the $PbI_2$•NMP structure by Raman spectra. i-j) ATR spectra of fingerprint regions for –C=N, –C-N and –C=O stretching vibrations. k) Illustration of the proposed crystallization process.

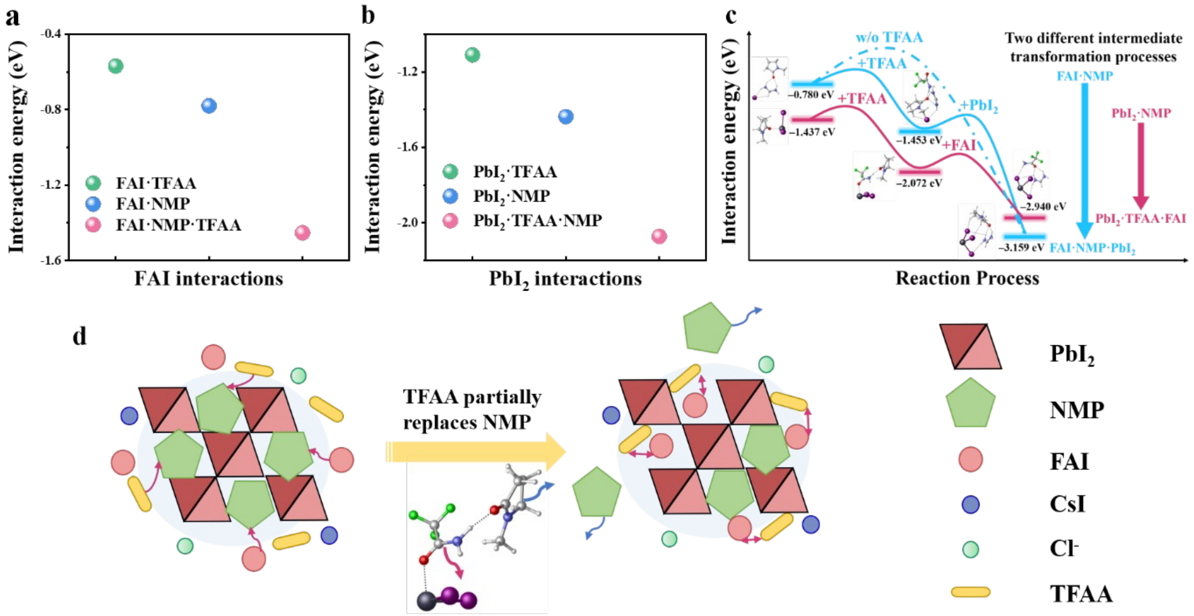

**Fig. 4.** Molecular interaction between perovskite precursors and additives by calculations. a-b) The perovskite species-FAI/PbI$_2$ interaction energies with the solvent (NMP) or additive molecule (TFAA). c) Schematic illustration of the interaction energies for forming FAPbI$_3$ intermediate phases with TFAA. d) Schematic illustration of TFAA partially replacing NMP.

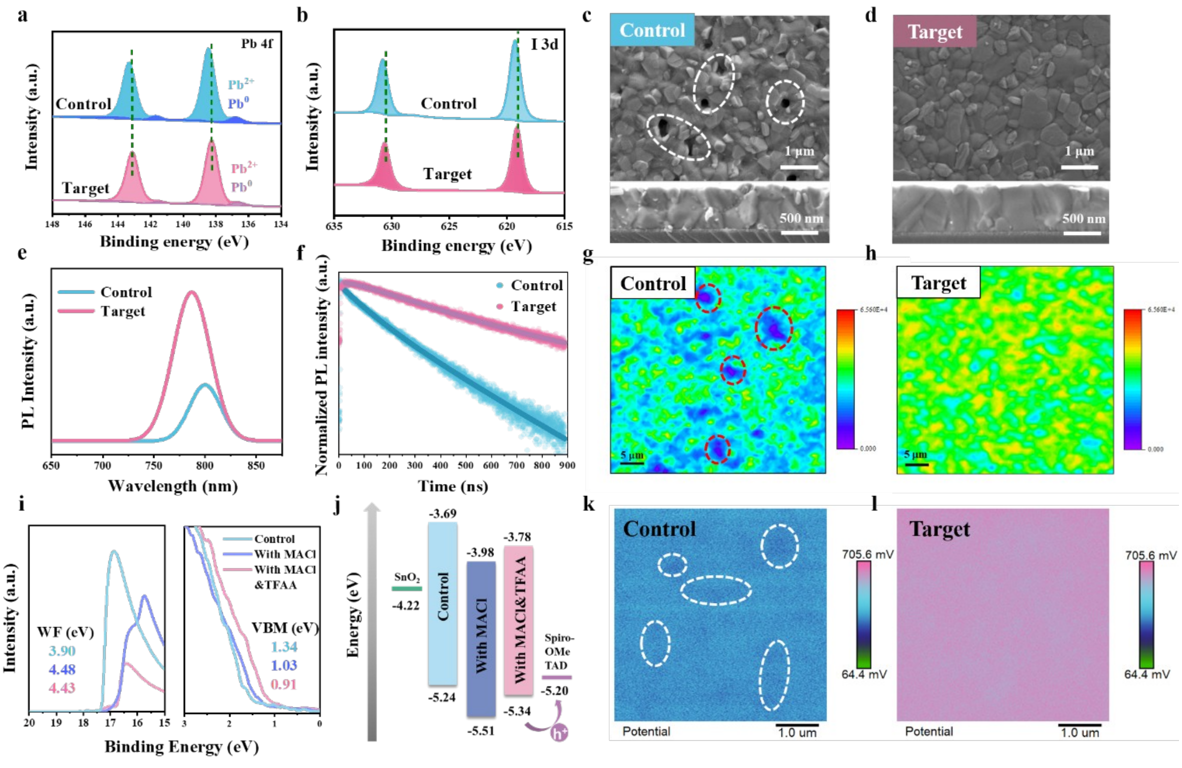

**Fig. 5.** Chemical homogeneity, defect passivation and energy-level alignment. a-b) XPS spectra of the core level I *3d* and Pb *4f* of the control and target film, respectively. c-d) Top-view and cross-sectional SEM images. e) Steady-state PL spectra and f) corresponding TRPL spectra for both samples. PL images of g) the control and h) the target perovskite films (the scale bar is 5 μm). Perovskite films were deposited on ITO substrates. i) cut-off edge and valence band in UPS spectra, and j) the energy diagram showing the energy levels extracted from the UPS data for the different perovskite films. k-l) Surface potential mapping by KPFM measurements.

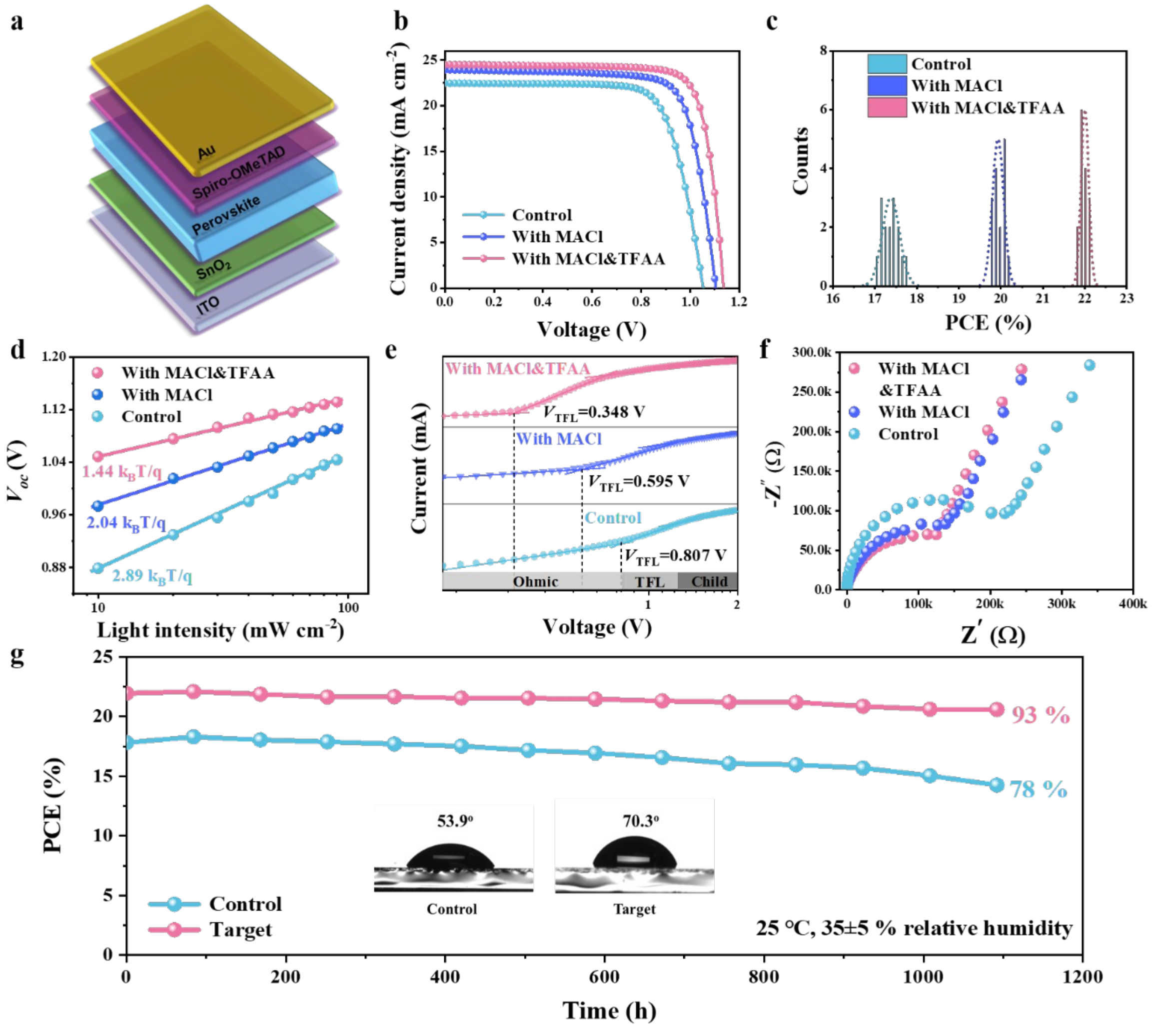

**Fig. 6.** Effect of additives on photovoltaic performance. a) Schematic illustration of PSCs with an n-i-p structure. b) *J-V* curves of best performed perovskite devices of different conditions with an active area of 0.04 $cm^2$. c) PCE distribution histograms of the devices with different modifications. d) Voltage dependence of light intensity. e) The SCLC measurements with a structure of ITO/PTAA/perovskite/Spiro-OMeTAD/Au. f) Nyquist plots measured in the dark. g) The stability test of the control and target PSCs stored in air environment, with the inset showing the contact angles of control and target perovskite films.

**Bo Zhou** received his B.S. degree at College of Chemistry and Chemical Engineering, Xiamen University in 2019. He is currently a Ph.D candidate at Dalian Institute of Chemical Physics, Chinese Academy of Sciences. His research mainly focuses on Pb-free perovskite solar cells.

**Pei Zhao** received her Ph.D. at Xi'an Jiaotong University in 2018, supervised by Prof. Xiang Zhao. She started the postdoctoral research in the group of Prof. Masahiro Ehara at Institute for Molecular Science, and became a Research Assistant Professor in 2022. Her research focuses on investigating electronic structures of complex systems to understand the bonding features, optical properties and catalytic activities through theoretical calculations.

**Junxue Guo** is currently a joint Ph.D candidate at University of Science and Technology of China and Dalian Institute of Chemical Physics, Chinese Academy of Sciences. She received her B.S. degree at Liaocheng University in 2019. Her current research focuses on the interface engineering of perovskite solar cells.

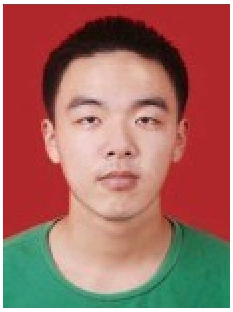

**Yu Qiao** received his B.S. degree at Lanzhou University in 2019. He is currently a Ph.D candidate at Dalian Institute of Chemical Physics, Chinese Academy of Sciences. His research mainly focuses on organic solar cells.

**Shuaifeng Hu** is currently a post-doctoral researcher at University of Oxford. He received his M.S. and Ph.D. degree at Huazhong University of Science and Technology in 2019 and Kyoto University in 2023, respectively. His general research interest focuses on fabricating well-performing p-i-n perovskite solar cells with a particular interest in narrow-bandgap mixed Sn–Pb perovskite solar cells and perovskite-containing tandem photovoltaics.

**Xin Guo** received his Ph.D. degree from the Changchun Institute of Applied Chemistry, Chinese Academy of Sciences (CAS) in 2009 then moved to the Max Planck Institute for Polymer Research in Mainz, Germany as a postdoc, where he was granted an Alexander von Humboldt Fellowship. From 2013–2015, he worked as a Research Associate in the Johns Hopkins University in Baltimore, USA. He was then appointed to be a full professor at the Dalian Institute of Chemical Physics, CAS. His research interests include (1) organic/polymer semiconducting materials and devices, (2) perovskite solar cells, and (3) molecular switches.

**Jiewei Liu** received her Bachelor's degree from Tsinghua University at 2012. He got Ph.D. degree from University of Oxford in 2016. From 2017 to 2020, he served as a postdoctoral fellow at the Institute for Chemical Research (ICR), Kyoto University. Then he joined the Dalian Institute of Chemical Physics in 2020, and was promoted to associate professor. His research interests: (1) Understanding and improving photovoltaic devices based on metal halide perovskite absorbers; (2) Developing efficient and stable lead-free perovskite as environmentally friendly photovoltaic material.

**Can Li** received his Ph.D. degree at Physical Chemistry from Dalian Institute of Chemical Physics, Chinese Academy of Sciences in 1989. He joined the same institute and was promoted to full professor in 1993. He was the President of the International Association of Catalysis Societies (2008–2012). Currently, he is the director of the Dalian National Laboratory for Clean Energy. His research interests include (1) UV Raman spectroscopy and ultrafast spectroscopy; (2) environmental catalysis and green catalysis; (3) heterogeneous asymmetric catalysis; and (4) solar energy utilization.